REPORT DOCUMENTATION PAGE

AFRL-SR-AR-TR-05-

0389

1. REPORT DATE (DD-MM-YYYY) 14-08-2005	2. REPORT TYPE Final Technical Report	3. DATES COVERED (From - To) 15 Oct 2004 – 14 Jul 2005

4. TITLE AND SUBTITLE Low-Noise Avalanche Photodiodes for Midwave Infrared (2 to 5 um) Applications	5a. CONTRACT NUMBER FA9550-05-C-0007
	5b. GRANT NUMBER
	5c. PROGRAM ELEMENT NUMBER
6. AUTHOR(S) Dr. Mark Itzler, Principal Investigator Princeton Lightwave Inc.	5d. PROJECT NUMBER
	5e. TASK NUMBER
	5f. WORK UNIT NUMBER

7. PERFORMING ORGANIZATION NAME(S) AND ADDRESS(ES) Princeton Lightwave Inc. University of Texas at Austin 2555 US Route 130 South Office of Sponsored Projects Cranbury, NJ 08512-5421 P.O. Box 7726 Austin, Texas 78713-7726	8. PERFORMING ORGANIZATION REPORT NUMBER

9. SPONSORING / MONITORING AGENCY NAME(S) AND ADDRESS(ES) USAF, AFRL AF Office of Scientific Res. 4015 Wilson Blvd, Room 713 Arlington, VA 22203-1954 NE	10. SPONSOR/MONITOR'S ACRONYM(S) AFOSR/NE
	11. SPONSOR/MONITOR'S REPORT NUMBER(S)

12. DISTRIBUTION / AVAILABILITY STATEMENT
Approved for public release; distribution unlimited

13. SUPPLEMENTARY NOTES

14. ABSTRACT
Report developed under STTR contract for topic AF04-T021. We have developed a mid-wave
infrared (MWIR) avalanche photodiode (APD) based on a GaInAs/GaAsSb superlattice absorption
region that is compatible with InP substrates. This superlattice structure exhibits a
photodetection cutoff wavelength of ~2.5 microns when lattice-matched to InP, and our
calculations show the introduction of compensated strain can provide cutoff wavelengths as
long as ~5 microns. Using the lattice-matched superlattice in a p-i-n structure, we have
demonstrated 43% quantum efficiency at 2.23 microns, a low dark current density of 1E-5
A/cm^2, and a peak detectivity of 7E10 cm√Hz/W, all at a temperature of 200 K, accessible
using thermoelectric coolers. By incorporating this superlattice into an APD structure with
an InP multiplication region, we have fabricated 160 micron diameter MWIR APDs exhibiting a
gain of 50 and an operating dark current of less than 100 nA at 240 K. Smaller 36 micron
diameter devices of the same structure exhibit sub-nanoampere dark currents below ~225 K.

15. SUBJECT TERMS
STTR Report

16. SECURITY CLASSIFICATION OF:			17. LIMITATION OF ABSTRACT	18. NUMBER OF PAGES	19a. NAME OF RESPONSIBLE PERSON Mark Itzler
a. REPORT UNCLASSIFIED	b. ABSTRACT	c. THIS PAGE	UL		19b. TELEPHONE NUMBER (include area code) 609-495-2551

Contract No.: FA9550-05-C-0007
Program Title: "Low-noise Avalanche Photodiodes for Midwave Infrared (2 to 5 µm) Applications"
Contractor: Princeton Lightwave Inc.
Principal Investigator: Mark Itzler

Final Report: 14 August 2005

1. Phase I Project Objectives

Our objectives for Phase I of this STTR program were to demonstrate:
  (1) a viable absorption layer structure for high performance photodetection in the mid-wave infrared (MWIR) spectral range,
  (2) a high performance avalanche multiplication region compatible with the MWIR absorber, and
  (3) an initial prototype of a separate absorption and multiplication (SAM) MWIR APD design based on the chosen absorber and multiplication regions.

To satisfy Objective (1), we targeted Sb-based materials showing promise for high-performance MWIR absorption. Our strategy was to work with absorbers based on $Ga_xIn_{1-x}As/GaAs_ySb_{1-y}$ Type-II heterostructures, and specifically, we have demonstrated a superlattice based on alternating layers of $Ga_{0.47}In_{0.53}As$ and $GaAs_{0.51}Sb_{0.49}$ that is lattice-matched to InP substrates and exhibits a cutoff wavelength of ~2.5 µm. We have also performed modeling which shows that with the introduction of compensated strain into the GaInAs/GaAsSb superlattice, we can extend the absorber cutoff wavelength to nearly 5 µm to cover the entire MWIR spectral range.

Because the GaInAs/GaAsSb superlattices chosen for the absorption layer are compatible with InP substrates, Objective (2) can be met through the use of well-established InP-lattice-matched avalanche multiplication regions such as bulk InP, bulk AlInAs, and InP-based impact ionization engineered structures.

Combining the results obtained for Objectives (1) and (2), we have met Objective (3) by demonstrating functional MWIR APDs that have been characterized over a temperature range of 200 – 300 K. Using the GaInAs/GaAsSb absorption region with a 2.5 µm cutoff wavelength, we have fabricated and characterized two APD structures: (i) an electron injection structure based on a bulk AlInAs multiplication region, and (ii) a hole injection structure based on a bulk InP multiplication region. Both of these device structures were fabricated into mesa geometry APDs. Additionally, because the hole injection structure is compatible with the fabrication of planar geometry devices, we also grew epitaxial APD structures for creating planar diffused junction devices that promise to provide lower surface leakage and long-term high reliability.

The remainder of this Final Report includes the following sections:
  2. Phase I Results on GaInAs/GaAsSb Type-II Heterostructure p-i-n Photodetectors
  3. Phase I Results on GaInAs/GaAsSb MWIR Avalanche Photodiode (APD) Devices
  4. Modeling of GaInAs/GaAsSb Type-II Heterostructure using Model Solid Theory
  5. Technological Feasibility of MWIR APDs based on InP Substrates
In these sections, we address the work performed and results obtained from our program activities.

20050901 061

2. Phase I Results on GaInAs/GaAsSb Type-II Heterostructure p-i-n photodetectors

2.1 Summary of Phase I p-i-n photodetector results

The bulleted list below summarizes the key Phase I performance achievements specifically related to the development of GaInAs/GaAsSb superlattice absorbers:

- Dark current densities of approximately 5 mA/cm^2 and 10 μA/cm^2 at 295K and 200K, respectively, for a 64 μm diameter $Ga_{0.47}In_{0.53}As/GaAs_{0.51}Sb_{0.49}$ p-i-n photodiode.

- A calibrated external quantum efficiency of 43% at 2.23 μm

- Specific detectivities as high as 7x10^{10} cm-Hz$^{1/2}$/W at 200 K

A detailed discussion of these results is presented in the following sub-sections.

2.2 Approaches to Longer Wavelength Detection on InP substrates

Previous work on extending the detection wavelength possible on InP substrates has focused on adding nitrogen to GaInAs[1,2] or using strain-compensated GaInAs quantum wells[3]. These efforts have led to emission/detection wavelengths of 2.04 μm and 1.9 μm, respectively.

The approach we selected to pursue in Phase I for extending the absorption region cutoff wavelength is based on a superlattice consisting of $Ga_xIn_{1-x}As$ and $GaAs_ySb_{1-y}$. The band structure for this superlattice is shown in Figure 1, where in the particular superlattice illustrated, the GaInAs and GaAsSb layers are both lattice-matched to InP.
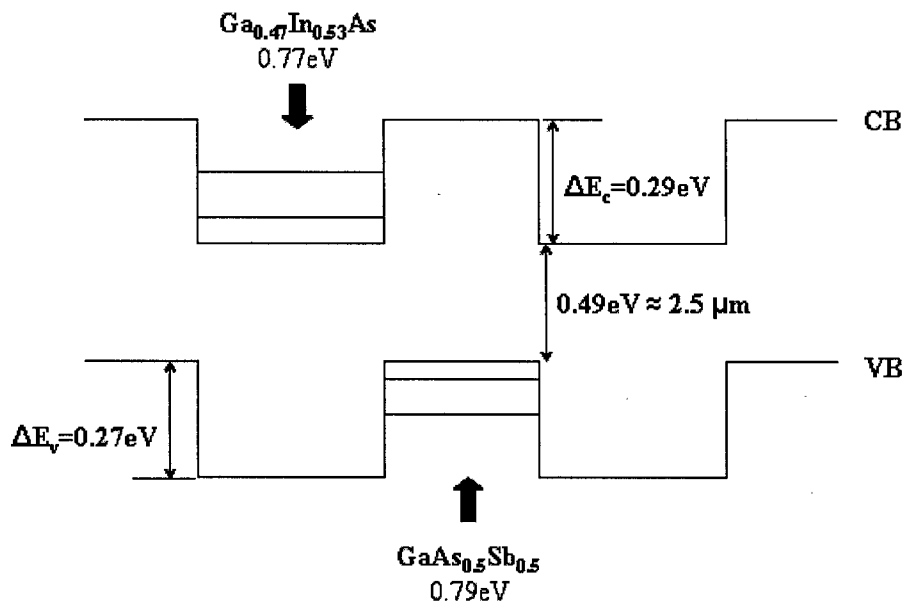

Figure 1: Calculation of the band lineup between lattice-matched GaAsSb and GaInAs on an InP substrate using the Model Solid Theory[4].

Optical transitions for this heterostructure occur between the valence band in the GaAsSb and the conduction band of GaInAs. Thus, the detection wavelength is not a direct function of the band gaps of the GaInAs and GaAsSb used. This provides a number of advantages for MWIR

detection. First, a large (> 0.7 eV) direct band-gap for both GaInAs and GaAsSb should lead to a lower thermal carrier generation rate than a material with a direct band gap related to the cutoff wavelength (in this case, 0.49 eV). This should result in a significant reduction in dark currents. Second, the variation of layer thickness and the addition of strain compensation between the two layers can be used to tune the detection cutoff wavelength to longer wavelengths since these design inputs affect the formation of mini-bands in the superlattice structure and dictate the resulting effective bandgap. This flexibility to customize the detector cutoff wavelength using straightforward superlattice design modifications is a tremendous benefit of the superlattice approach. The GaInAs/GaAsSb superlattice structure will be described in greater detail below in the section covering Phase I modeling using the Model Solid Theory[4].

2.3 MBE Growth of GaInAs/GaAsSb Type-II Heterostructures

MBE growth is normally carried out under a group-V overpressure (i.e. V/III ratio > 1). Under these conditions, the sticking coefficient of group-III atoms is very close to unity. However, the group-V atoms of different species have to compete for a limited number of anion sites. This leads to a strong dependence of the alloy composition on the growth conditions. Antimony incorporation in III-AsSb is strongly dependent on the various growth parameters, namely, substrate temperature, group III growth rates, and As and Sb beam equivalent pressures (BEPs). We studied this dependence by growing $GaAs_ySb_{1-y}$ strained quantum wells (QWs) on GaAs, and $GaAs_ySb_{1-y}$ and $AlAs_ySb_{1-y}$ bulk layers on InP. We observed that with increasing growth temperature, the Sb incorporation in the films decreases because of increased Sb desorption from the substrate at higher growth temperatures. Sb incorporation was also seen to increase with increasing group-III growth rate. This suggests that at higher group-III growth rates, there are more cations available for Sb adatoms to bond with, which keeps the Sb atoms from desorbing from the surface. For the growth of both GaAsSb and AlAsSb, As seemed to incorporate preferentially over Sb. Good lattice matching of $AlAs_{0.55}Sb_{0.45}$ and $GaAs_{0.51}Sb_{0.49}$ on InP was observed at both As and Sb BEPs of approximately 3.0×10^{-6} torr.

A modified Varian Gen-II solid-source MBE reactor, equipped with Al, Ga, and In effusion cells, and As, P, and Sb valved crackers was used to grow the structures. Si and Be effusion cells were used to provide the dopants. As and Sb beam equivalent pressures, determined by an ion gauge and regulated by the valved crackers, were used to calibrate the compositions of III-AsSb materials. Substrate temperature prior to and during the growth was determined by an optical pyrometer. Optimal growth temperature was determined by comparing the PL intensity and peak width of samples grown at different temperatures. For both strained GaAsSb on GaAs, and lattice-matched GaAsSb on InP, the optimal growth temperature was found to be about 525°C. For the growth of GaInAs/GaAsSb SLs, brief pauses were introduced between layers whenever group-V flux needed to be changed. We have determined from previous experiments that such short pauses lead to reasonably abrupt and high quality interfaces. Crystal composition and quality were confirmed using high-resolution x-ray diffraction (HRXRD).

2.4 GaInAs/GaAsSb p-i-n Diode Device Structure and Fabrication

To demonstrate long wavelength light absorption using Type-II SLs, we designed a p-i-n photodiode structure with 500nm thick Si-doped $Ga_{0.47}In_{0.53}As$ and 500nm thick Be-doped $Ga_{0.47}In_{0.53}As$ as the n- and p-layers, respectively. The i-region of this photodiode contained 150

pairs of $Ga_{0.47}In_{0.53}As(5nm)/GaAs_{0.51}Sb_{0.49}(5nm)$ quantum wells lattice-matched to InP. A schematic diagram of the device structure is shown in Figure 2.

| 500 nm p-
$Ga_{0.47}In_{0.53}As$ |
| 45 nm $Ga_{0.47}In_{0.53}As$ |
| type-II QWs
150 pairs |
| 50 nm $Ga_{0.47}In_{0.53}As$ |
| 500 nm n-
$Ga_{0.47}In_{0.53}As$ |
| N-type InP
substrate |

$GaAs_{0.51}Sb_{0.49}$
$Ga_{0.47}In_{0.53}As$
$GaAs_{0.51}Sb_{0.49}$
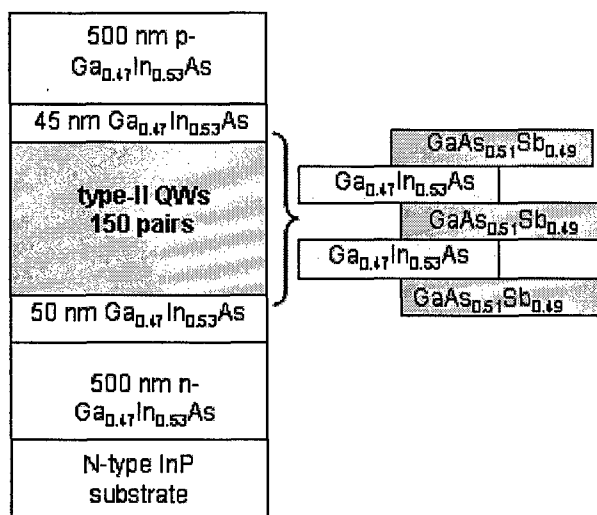$Ga_{0.47}In_{0.53}As$
$GaAs_{0.51}Sb_{0.49}$

Figure 2: Schematic of the p-i-n device structure using a GaInAs/GaAsSb Type-II superlattice as the absorption region.

Mesa devices of different diameters were fabricated using standard photolithography and wet etching techniques. An etch chemistry of $H_3PO_4:H_2O_2:H_2O$ (1:1:10) was used for both GaInAs and GaAsSb. Silicon dioxide was used to passivate the mesa walls to minimize edge leakage currents. Ti/Pt/Au and AuGe/Ni/Au were deposited for p- and n-metal contacts using photolithography and liftoff techniques. Electroplated Au air-bridges were used to connect the p-metal from the mesa tops to the p-pads. N-pads were deposited directly on the n-metal contacts. Devices were contacted by wire-bonding to the p- and n- pads.

2.5 Current-Voltage Characteristics for GaInAs/GaAsSb p-i-n diodes

Room temperature I-V characteristics were measured using an Agilent 4156B semiconductor parameter analyzer. Dark current density at a reverse bias of 1 V was less than 5 mA/cm^2 at room temperature. Dark current data from devices of different diameters showed a good quadratic fit to the device diameter. This scaling of the dark current with device area implies that most of the dark current is generated in the bulk of the devices with negligible contribution from edge leakage. To further understand the mechanisms contributing to the dark current, I-V measurements were taken at different temperatures. Dark I-V curves at temperatures from 200 K to 295 K are plotted in Figure 3.

For these devices, the dark current at low bias drops rapidly with temperature; this is representative of thermal generation dominating the dark current in the low-bias regime. High-bias dark current has a relatively weaker dependence on temperature, representative of tunneling dark current. Low-bias dark current was plotted against 1/T, and the activation energy for thermal generation of carriers was calculated from a linear fit to the data; see Figure 4. The activation energy at a reverse bias of 2 V was calculated to be 0.326 eV. This energy is near the mid-bandgap energy of both $Ga_{0.47}In_{0.53}As$ (0.77 eV at 293 K) and $GaAs_{0.51}Sb_{0.49}$ (0.79 eV at 293 K), suggesting that generation through mid-gap traps is the dominant contributor to dark current at this bias[5]. The possibility that this leakage mechanism through mid-gap states of the constituent superlattice materials remains the dominant leakage mechanism for longer cutoff wavelength

superlattice compositions is very promising for achieving exceptionally low dark current with longer wavelength detectors based on this platform.
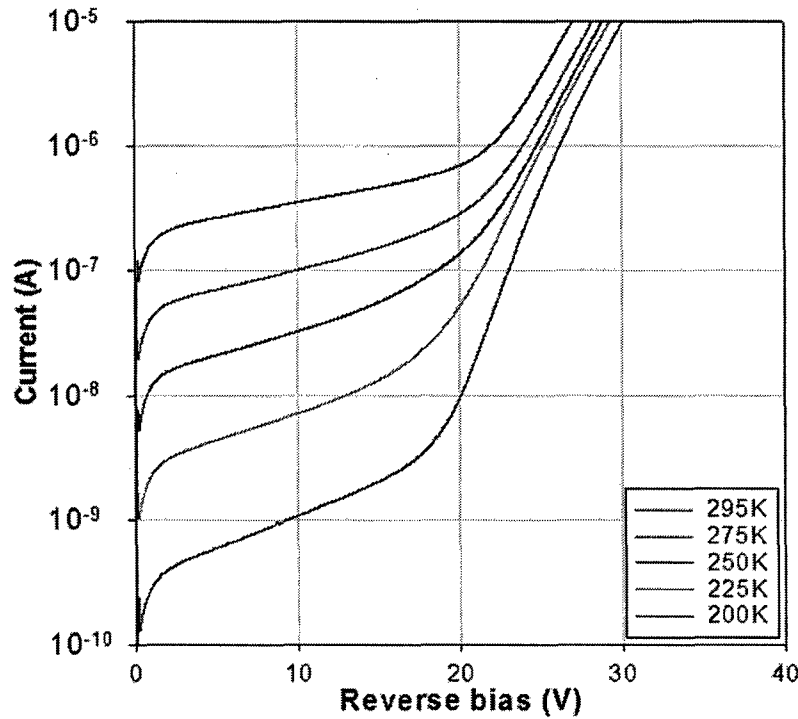

Figure 3: Dark current vs. voltage from a 64µm diameter p-i-n device based on a GaInAs/GaAsSb superlattice lattice-matched to an InP substrate, measured at different temperatures between 200 and 295 K.
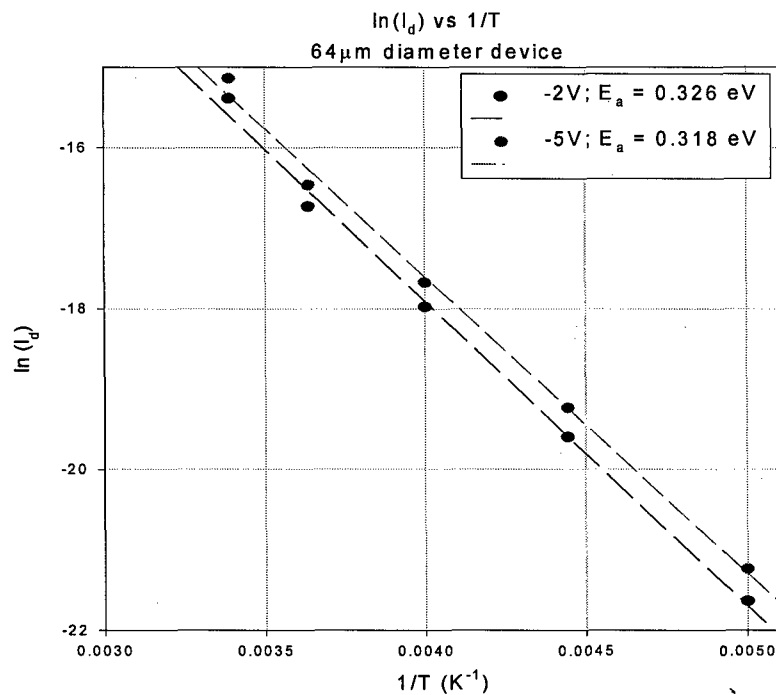

Figure 4. Linear behavior of dark current (see Fig. 3) versus 1/T indicates that leakage is dominated by thermal generation of carriers. Extracted activation energies at -2 and -5 V are close to mid-gap states of GaInAs and GaAsSb, consistent with generation-recombination current leakage.

2.6 Quantum Efficiency and Detectivity

Spectral response of the device was measured using a Nicolet Magna-II FTIR spectrometer and a current pre-amplifier. Since reporting preliminary results in interim reports for this program, we have taken considerable care to improve the measurement accuracy and greatly reduce any remaining errors in the measurements. The FTIR response of the GaInAs/GaAsSb photodiode was measured through a 1800 nm long-pass filter using a black-body source held at 1000° C. This helped to remove the noise from the FTIR below 1.7 µm. To account for variations in the black body source, two calibrated detectors were measured (PbS and relaxed GaInAs) in the system, and the results were used to calibrate the results for our detectors. The calibration curves for the PbS and relaxed GaInAs detectors lead to similar results for the GaInAs/GaAsSb photodiodes. Figure 5 shows the normal incidence photoresponse of the device at a reverse bias of 2 V as a function of temperature.
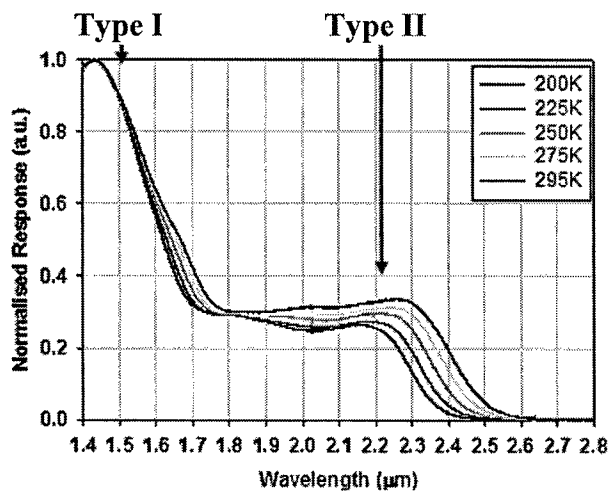

Figure 5: Normalized FTIR response for a 64 µm diameter GaInAs/GaAsSb photodiode at 2 V reverse bias.
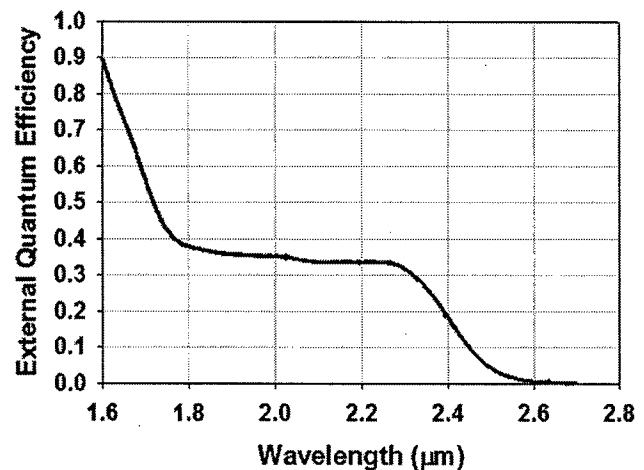
Figure 6: Room temperature quantum efficiency as a function of wavelength. The quantum efficiency at 2.26 µm was 34%, and response was observed beyond 2.5 µm.

The Type-I (spatially direct) peaks from $Ga_{0.47}In_{0.53}As$ and $GaAs_{0.51}Sb_{0.49}$ QWs are seen just below 1.5µm, and the type-II (spatially indirect) response is apparent from 1.7µm to 2.5µm. As expected, the peaks red-shift with an increase in temperature. The response magnitude also increases with temperature due to photogenerated carriers having more energy to escape out of the QWs and contribute to collected photocurrent at the electrodes. The room temperature quantum efficiency spectrum is shown in Figure 6. This quantum efficiency was increased by the improvement of the dielectric coating on the optically active area, as described below.

Specific detectivity (D*) as a function of wavelength was calculated from the responsivity and dark noise current data (not shown). The measured noise current drops rapidly with temperature down to 225K. Below 225K, the drop of noise current with temperature is reduced substantially. The range of rapid reduction in the noise current is within the cooling range of a multi-stage thermoelectric (TE) cooler. This low dark noise leads to high specific detectivity (D*) values despite the reduced responsivity at lower temperatures. The D* vs. temperature data is shown in Figure 7. The peak Type-II detectivity (D*) at room temperature was 3.8×10^9 cm-Hz$^{1/2}$/W. Peak type-II detectivity (D*) at 275K and 200K were 1×10^{10} cm-Hz$^{1/2}$/W and 5.6×10^{10} cm-Hz$^{1/2}$/W, respectively. The rollover in D* is due to the slower reduction in noise current below 225K.
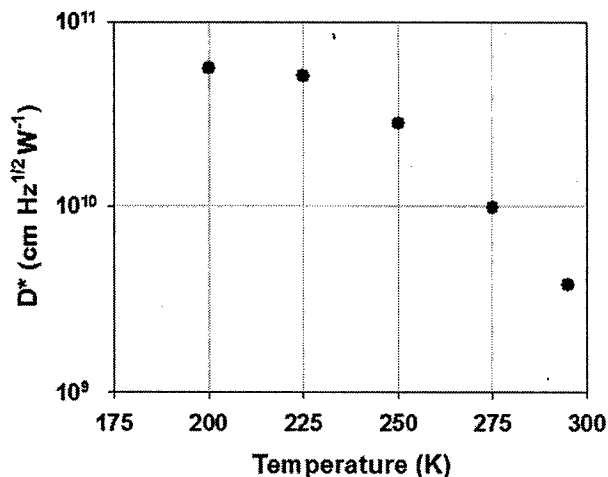
Figure 7: Specific Detectivity D* for a 64 μm diameter GaInAs/GaAsSb SL photodiode as a function of temperature.
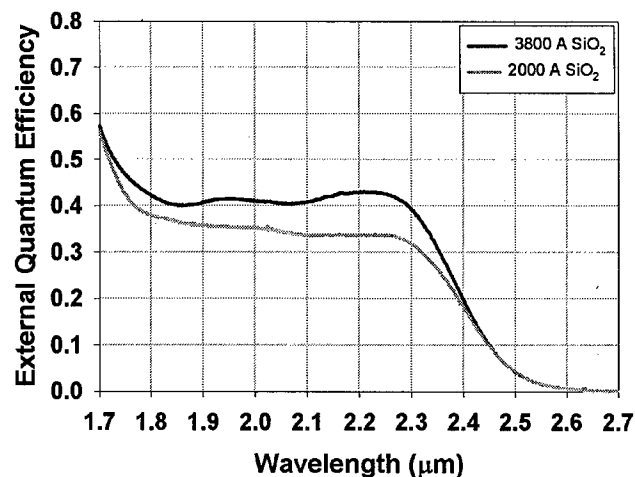
Figure 8: Initial peak external quantum efficiency of 34% at 2.23 μm for a device with a non-optimized anti-reflection coating of 2000 Å SiO$_2$ was improved to 43% at 2.26 μm by increasing the coating thickness to 3800 Å.

The data presented in Figures 5 and 6 was obtained for a device that had a coating of 2000 Å of SiO$_2$ on the top surface, which results in approximately 20% back reflection of 2 μm to 2.5 μm wavelength incident light. In order to improve the coupling of incident light, an additional 1800 Å of SiO$_2$ was deposited to provide a more optimized anti-reflection (AR) coating on the top facet of the detector. The calculated reflectivity from the top surface with 3800 Å of SiO$_2$ is approximately 0.05 at 2.3 μm wavelength. The addition of this improved AR coating led to peak external quantum efficiency of 43% at 2.23 μm. The room temperature external quantum efficiency vs. wavelength curves for a device with the non-optimized (2000 Å) and optimized (3800 Å) coatings are shown in Figure 8. Improved AR-coating led to a 22% increase in the measured external quantum efficiency. A commensurate increase in the detectivity values is expected for devices with the improved AR-coating, yielding a 200K detectivity of 7.1 x 10^{10} cm-Hz$^{\frac{1}{2}}$/W. Since the layers used for absorption in these devices are lattice-matched to InP, there is no theoretical upper limit to the number of layers grown, and further increase in quantum efficiency and detectivity can be achieved by incorporating more QWs in the absorption region.

3. Phase I Results on GaInAs/GaAsSb MWIR Avalanche Photodiode (APD) devices

3.1 Summary of Phase I MWIR APD device results

The bulleted list below summarizes the key Phase I performance achievements for MWIR APDs based on GaInAs/GaAsSb superlattice absorbers with a cutoff wavelength of 2.5 μm:

- Design, fabrication, and characterization of functional MWIR APDs based on both electron injection (bulk AlInAs) and hole injection (bulk InP) multiplication regions

- Demonstration of hole injection APD performance from 200 K to 300 K, including:
  - Gains in excess of 50 at 240 K
  - Dark current < 1 nA for 36 μm diameter device for temperatures ~ 225 K
  - Dark currents < 100 nA at 240 K and < 10 nA at 210 K for 160 μm diameter device

- Dependence on device dimensions of I-V characteristics for hole injection MWIR APDs obtained at room temperature, shows areal scaling with minimal perimeter leakage effects

A detailed discussion of these results is presented in the following sub-sections.

3.2 Incorporation of 2.5 μm GaInAs/GaAsSb superlattice absorber into full APD structure

Having demonstrated very promising performance for 2.5 μm cutoff $Ga_{0.47}In_{0.53}As/GaAs_{0.49}Sb_{0.51}$ type-II superlattice (SL) structures, along with a design path to reaching ~5 μm cutoff wavelengths, our focus progressed to the incorporation of the 2.5 μm cutoff SL into a fully functional APD structure. As we have stressed above, the fact that this SL heterostructure is compatible with the InP-lattice-constant materials system allows us to leverage the extensive experience we have in designing multiplication regions and full APD structures for InP-based APDs. We have identified at least three possible choices for the multiplication region design:

(i) electron injection structures based on bulk $Al_{0.48}In_{0.52}As$, which is lattice-matched to InP;

(ii) hole injection structures based on bulk InP; and

(iii) impact ionization engineered multiplication regions based on heterostructures designed with the InGaAlAs quaternary system, or with AlInAs/InP heterojunctions, both of with are lattice-matched to InP.

Our initial approaches have included choices (i) and (ii) using InAlAs and InP bulk multiplication regions, respectively.

3.3 Electron injection MWIR APD – AlInAs multiplication region

In Figure 9, we illustrate the design of an electron injection APD structure based on a 0.5 μm thick undoped AlInAs multiplication region. This device is designed to seed avalanche gain by electron injection because AlInAs more readily multiplies electrons than holes due to its larger impact ionization coefficient for electrons. The 0.6 μm $Ga_{0.47}In_{0.53}As/GaAs_{0.49}Sb_{0.51}$ SL absorber has fewer periods than the absorption region we demonstrated above in our p-i-n structure, but is otherwise identical in the design of the superlattice (i.e., each layer is 5 nm thick).

X-ray (004) rocking curve data for this wafer is shown in Figure 10. The satellite peaks from the superlattice are sharp with full-width at half maximum (FWHM) of about 60 arc seconds, implying high quality layers with abrupt interfaces and little or no compositional grading.

Initial characterization of the the electron injection APD shows proper APD functionality. In Figure 11, we present 295 K (room temperature) I-V characteristics obtained for dark and illuminated conditions. Punchthrough occurs at approximately 16 V, beyond which the device shows gain. The dark current at 295 K with this initial structure is rather high, but after subtracting the dark current from the I-V curve taken with illumination, we find a gain of about 5 at 40 V. We anticipate substantial improvement in device performance with cooling of the device to thermoelectric cooler-accessible temperatures on the order of 200 K. First, we have already shown in Figure 3 that upon cooling from 295 K to 200 K, dark current for this SL structure is reduced by a factor of 300 – 500. Moreover, for operation at 295 K, this structure does not contain enough doping in the AlInAs "charge" layer (see Figure 9) to maintain a low electric field in the SL absorption region. However, at lower temperatures, the breakdown field of the AlInAs multiplication region is reduced, so that at 200 K we should find substantially higher gains between 20 V and 40 V, relative to the 295 K performance, along with greatly reduced dark

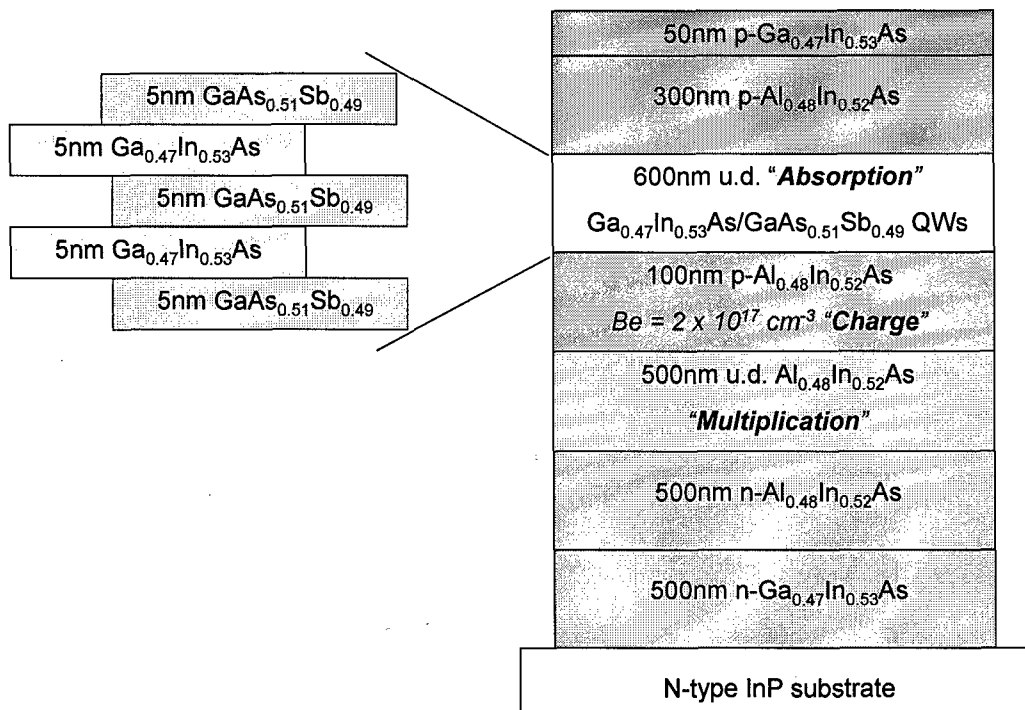current.　We will also discuss our approach to modelling this temperature-dependent gain behavior below.

5nm $GaAs_{0.51}Sb_{0.49}$	50nm p-$Ga_{0.47}In_{0.53}As$
5nm $Ga_{0.47}In_{0.53}As$	300nm p-$Al_{0.48}In_{0.52}As$
5nm $GaAs_{0.51}Sb_{0.49}$	600nm u.d. "*Absorption*" $Ga_{0.47}In_{0.53}As/GaAs_{0.51}Sb_{0.49}$ QWs
5nm $Ga_{0.47}In_{0.53}As$	100nm p-$Al_{0.48}In_{0.52}As$ $Be = 2 \times 10^{17}$ cm^{-3} "*Charge*"
5nm $GaAs_{0.51}Sb_{0.49}$	500nm u.d. $Al_{0.48}In_{0.52}As$ "*Multiplication*"
	500nm n-$Al_{0.48}In_{0.52}As$
	500nm n-$Ga_{0.47}In_{0.53}As$
	N-type InP substrate

Figure 9. Epitaxial structure for electron injection 2.5 µm cutoff InP-based APD employing a lattice-matched AlInAs multiplication region and GaInAs/GaAsSb superlattice absorber.
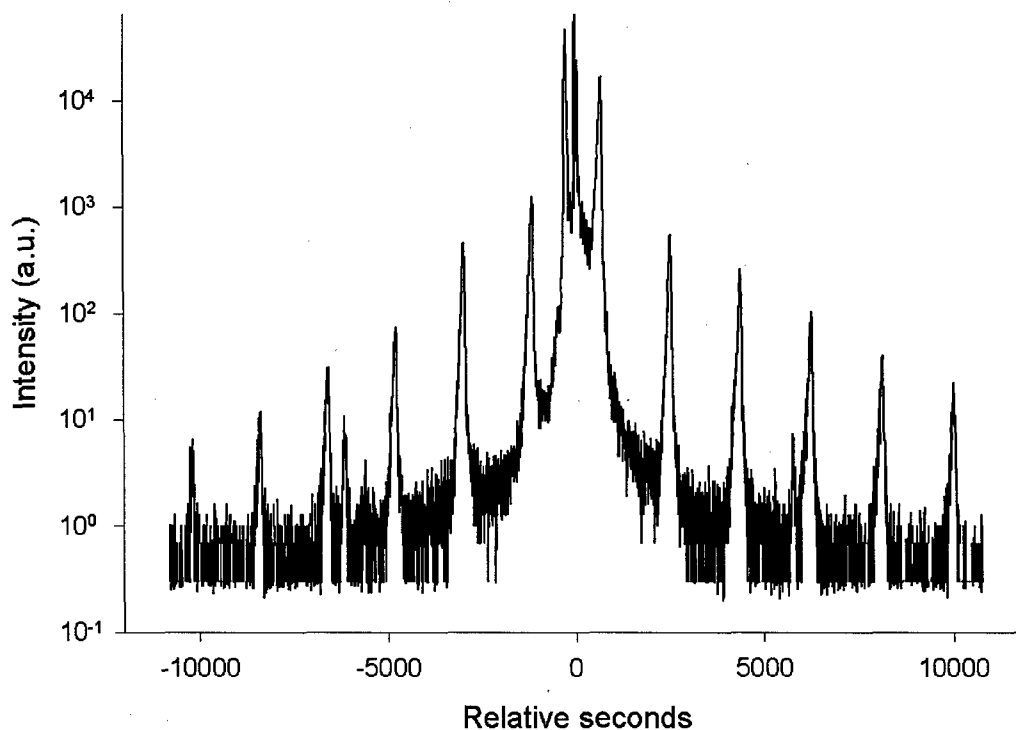
Fig. 10. X-ray rocking curve data for electron injection 2.5 µm cutoff InP-based APD epi-wafer.

P1091
Reverse I-V and Gain
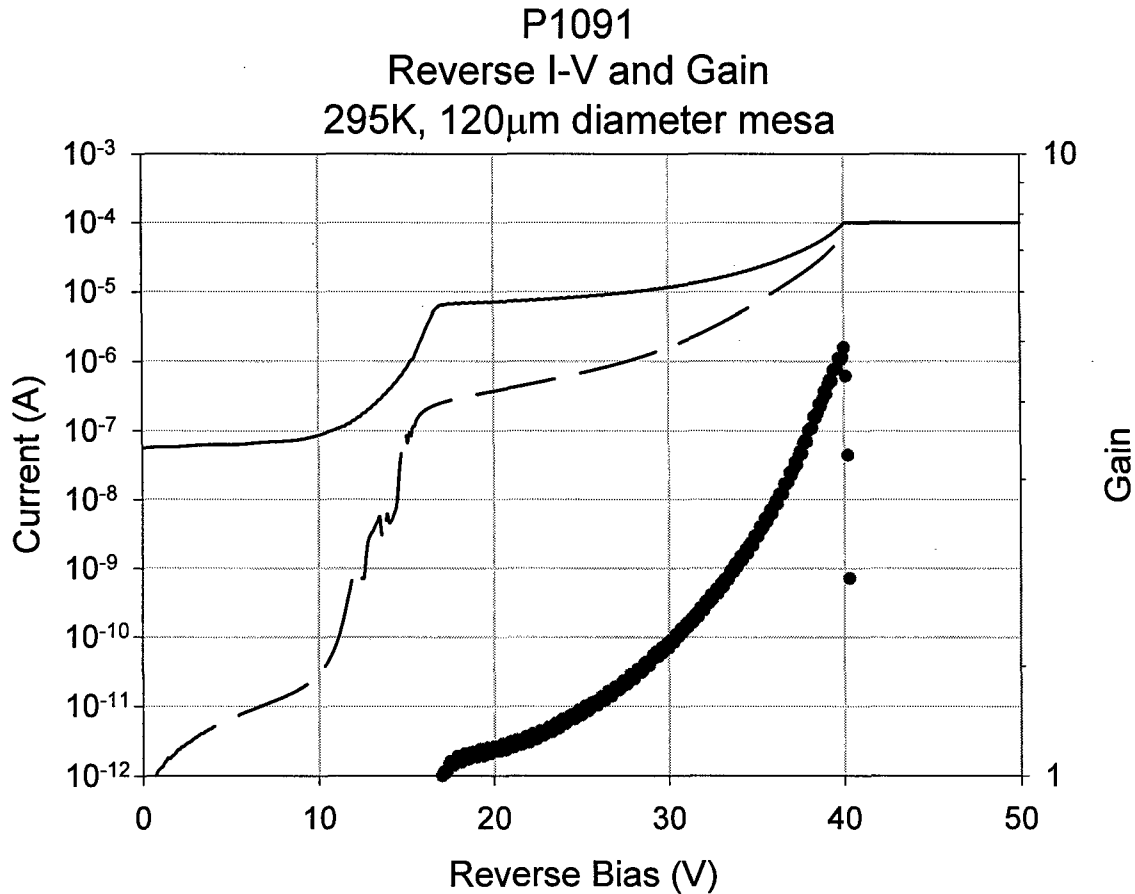## 295K, 120μm diameter mesa

Figure 11. Dark and illuminated I-V characteristics for an electron injection 2.5 μm cutoff InP-based APD. A gain of 5 is exhibited after dark current subtraction.

3.4 Hole injection MWIR APD – InP multiplication region

Accompanying the growth of the electron injection MWIR APD described in the last section, we have also completed the epitaxial growth of a hole injection MWIR APD with the structure presented in Figure 12. In this device, we use a 0.8 μm thick bulk InP multiplication region, which more readily multiplies holes than electrons due to a larger impact ionization coefficient for holes. The 1.5 μm thick SL absorption region is of an identical SL design to that used the electron injection design (and our earlier p-i-n demonstration devices), and the thin GaInAs and GaInAsP layers are used as "grading" layers to smooth out the rather large valence band discontinuity that would be created by growing the InP charge layer directly on top of the SL absorber.

We have carried out simulations of the hole injection structure to determine the internal electric field profile at breakdown, illustrated in Figure 13(a), as well as the gain dependence on voltage, shown in Figure 13(b). These simulations made use of a local field model that does not account for the history-dependence of the avalanche process, but this modelling approach has been shown to be sufficiently valid for wider multiplication layers such as the 0.8 μm layer used for this structure (see Figure 12).
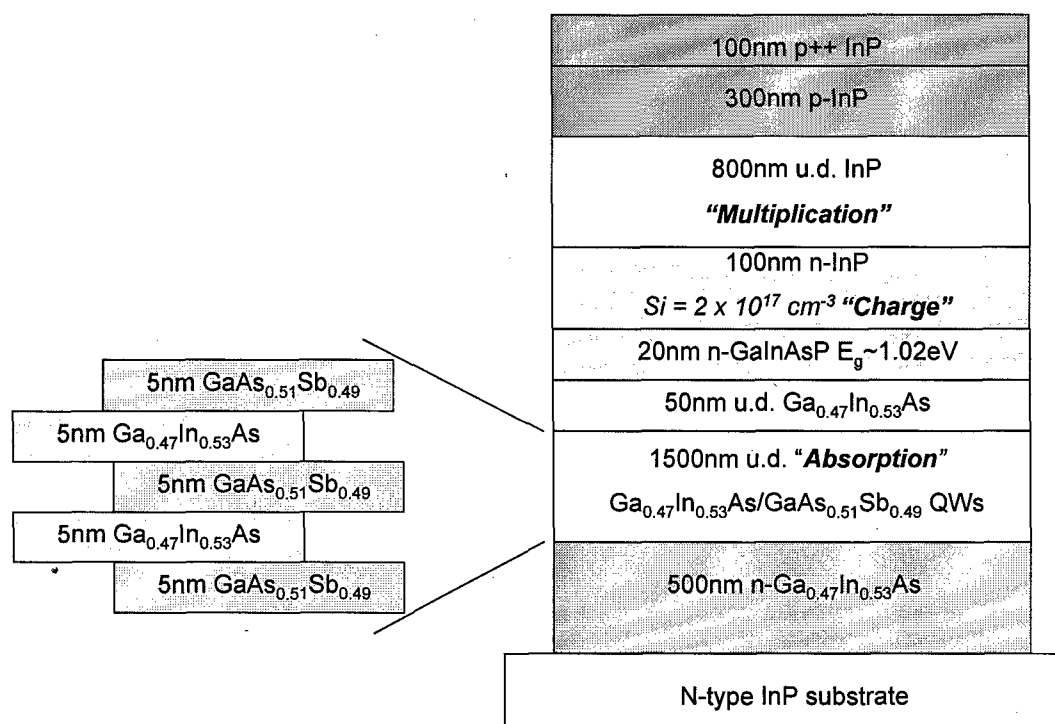
Figure 12. Epitaxial structure for hole injection 2.5 μm-cutoff InP-based APD employing a bulk InP multiplication region and a GaInAs/GaAsSb superlattice absorber.
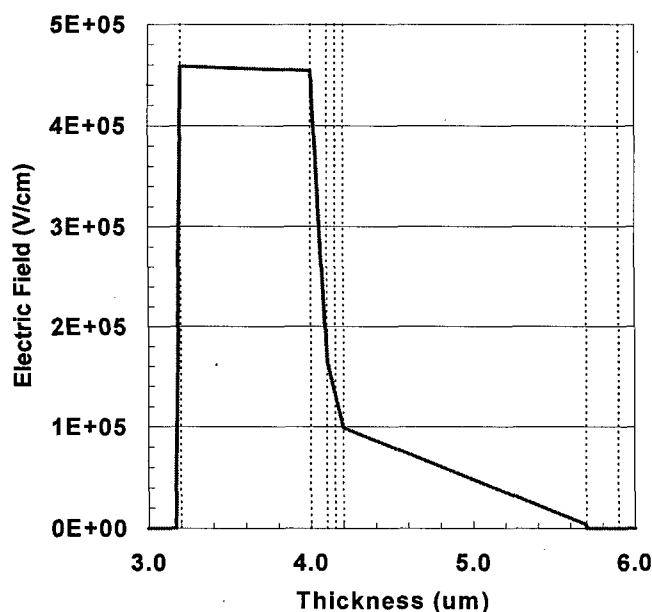

Fig. 13(a). Simulation of internal electric field at breakdown for the hole injection MWIR APD using a 0.8 μm InP multiplication region (see Figure 12).
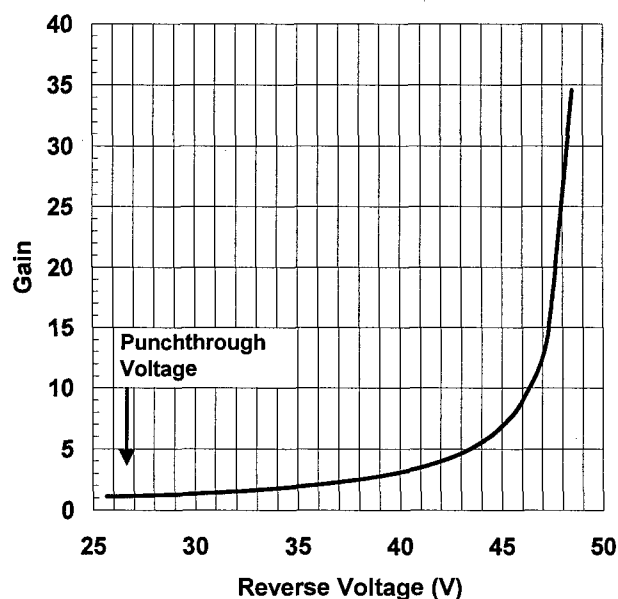
Fig. 13(b). Simulated gain vs. voltage curve for the hole injection MWIR APD using a 0.8 μm InP multiplication region (see Figure 12).

It is a well-established fact that multiplication regions with a smaller ratio of impact ionization coefficients provide lower noise and higher bandwidth performance for linear mode APDs. Since the electron injection avalanche material AlInAs has a smaller ratio α/β than the ratio β/α for the hole injection avalanche material InP, AlInAs should provide superior APD performance. However, the ability to implement our novel MWIR APD structure in a proven production device platform will be of very significant value in transitioning this early stage development work into near-term deployable products.

The well-passivated planar APD geometry based on dopant-diffused p-n junctions has shown much better long-term stability and reliability of performance than mesa geometry APDs, and the investigators at PLI have a decade of experience in fabricating near-infrared InGaAs/InP APDs based on a platform that involves p-dopant diffusions to form a buried p-n junction with a planar device geometry. This design platform can be applied to the hole injection structure shown in Figure 12 by simply replacing the InP multiplication region and the layers above it with a thick (e.g., ~4 μm) undoped InP layer. With a well-controlled diffusion (e.g., to ~0.1 μm accuracy) of an appropriate p-dopant material (e.g., Zn), we can create a multiplication region of any desired width by leaving a corresponding thickness of undoped InP. Shaping of the junction profile through the use of special techniques (such as multiple diffusions) is an effective approach for suppressing edge breakdown, and we have implemented this approach for large-volume production of NIR telecommunications APDs.

In principle, one could hope to implement a similar planar geometry with AlInAs multiplication regions, but because this material requires electron injection, the polarity of the entire structure must be inverted. This would require the use of an n-dopant for the diffused junction formation, and despite many years of InP-based photodiode development and production, no n-dopant has yet been demonstrated that would be compatible with this photodiode device platform.

Therefore, we have used the epitaxial structure based on an InP multiplication region illustrated in Figure 12 to process mesa geometry MWIR APDs for comparison with a similar structure to be implemented in a planar geometry. Results for the mesa devices are presented below, and the epi-wafer growth for the planar geometry device structure has been completed.

Initial results for our hole injection MWIR APD measured as a function of temperature are summarized by the dark I-V characteristics presented in Figure 14 and the gain vs. voltage curves presented in Figure 15 for a fairly large area 160 μm diameter mesa geometry APD. The dark current characteristics (Figure 14) show that there is sub-nA leakage for voltages less than the punchthrough voltage of ~36 V. Beyond punchthrough, dark currents are as low as ~10 nA at 210 K and ~100 nA at 240 K. The breakdown voltage of ~41 V at 210 K increases with increased temperature, as expected, to ~44 V at 240 K. In Figure 15, we show gain vs. voltage characteristics that demonstrate a gain of ~40 at 210 K and ~50 at 240 K. Because the punchthrough voltage is fairly high for these devices, there is already finite gain at punchthrough, as indicated by the finite slope of the gain vs. voltage curves at 36 V. We have estimated that the gain at this punchthrough voltage is approximately 2 in plotting these gain curves. Tailoring of the structure to achieve lower punchthrough voltages by reducing the field control charge will substantially reduce the uncertainty in the gain at punchthrough for future iterations of this structure.
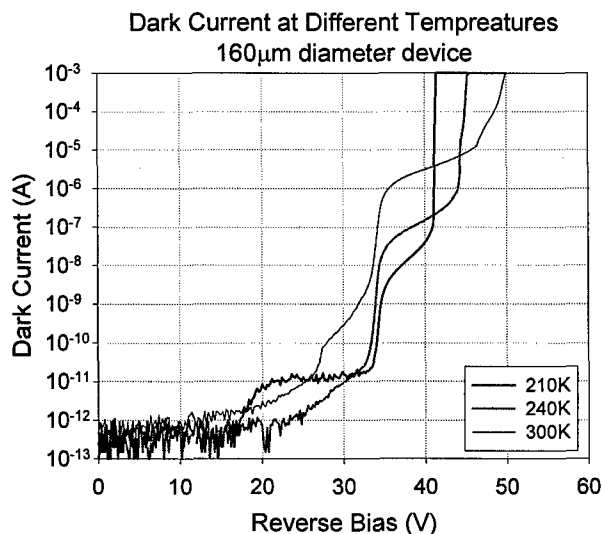
Dark Current at Different Tempreatures
160μm diameter device

Gain at Different Temperatures
160μm diameter device

Figure 14. Dark current characteristics for a hole injection MWIR APD with a 160 μm diameter mesa geometry at 210 K, 240 K, and 300 K. Punchthrough occurs at 36 V, and dark currents of less than 100 nA are found in the range of 210 – 240 K.
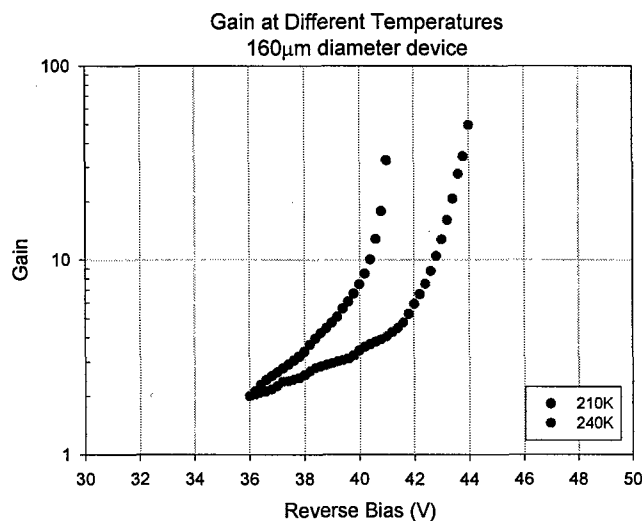
Figure 15. Gain vs. voltage characteristics for a hole injection MWIR APD with a 160 μm diameter mesa geometry at 210 K and 240 K. Gains of >40 are achieved before breakdown.

Further temperature-dependent dark current characteristics for our hole injection structure are illustrated in Figure 16 for a 36 μm diameter device fabricated from the same epitaxial structure used in making the 160 μm diameter device for which data was presented in Figure 14. For this smaller area detector, similar to the size of a single pixel in a typical focal plane array layout, Figure 16 shows that sub-nanoampere dark currents are achieved for temperatures below 225 K, easily accessible with thermoelectric cooling. Optical measurements on this device confirmed a spectral response comparable to that presented in Figure 5.
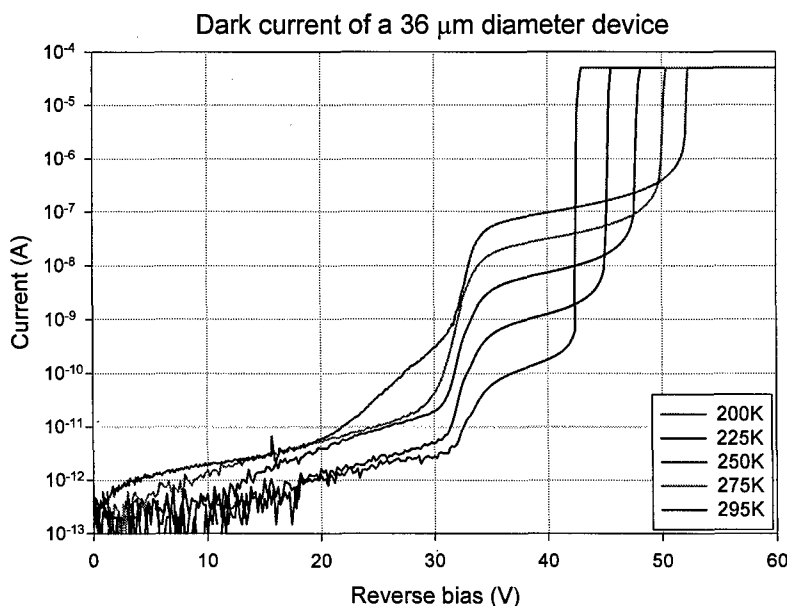

Dark current of a 36 μm diameter device

Figure 16. Dark I-V characteristics for a 36 μm diameter mesa geometry hole injection APD measured for temperatures between 200 K and 295 K.

We have also studied the room temperature I-V characteristics for the hole injection MWIR APD structure for device diameters varying from 36 to 88 μm (see Figure 17). Devices consistently showed gains up to about 40, and room temperature dark currents were on the order of 100 – 500 nA for the smaller diameters. Based on temperature-dependent data shown above, we expect to find reduction of these dark currents by a factor of at least 100 for operation below ~220 K.
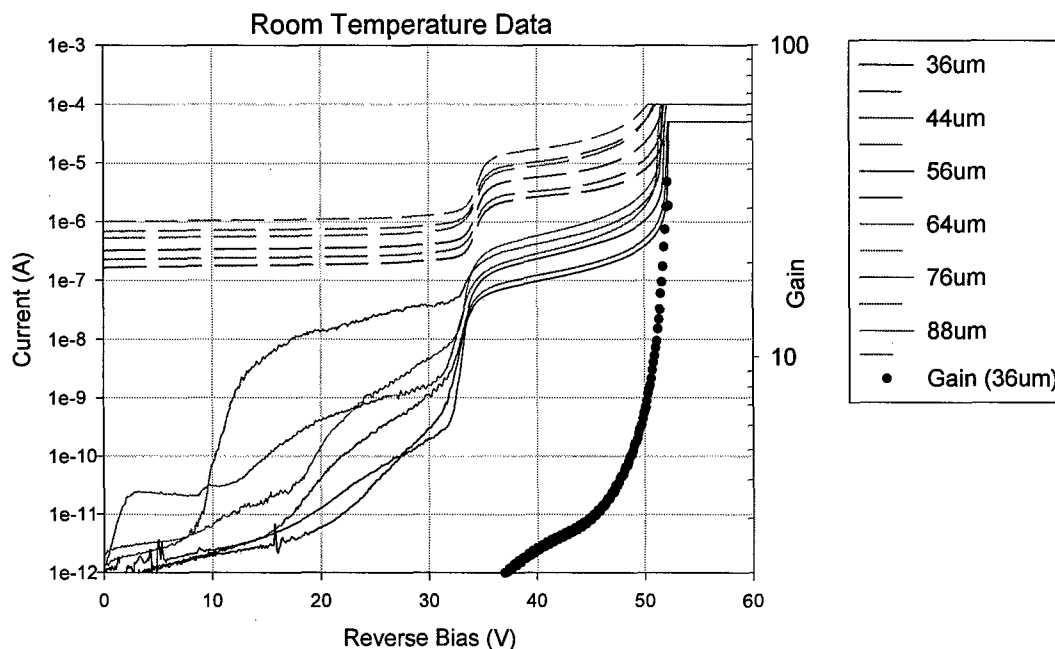
Figure 17. Room temperature dark current and photocurrent I-V characteristics for a hole injection MWIR APDs with mesa geometry device diameters ranging from 36 to 88 μm. Right-hand scale illustrates gain for the 36 μm diameter device.

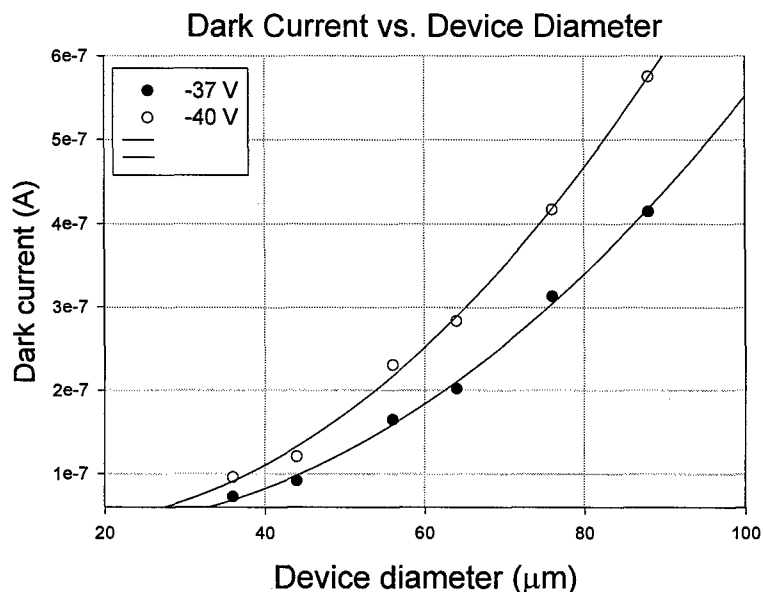**Figure 18.** Room temperature dark current plotted as a function of device diameter for the data presented in Figure 3 for hole injection MWIR APDs with mesa geometry device diameters ranging from 36 to 88 μm. Quadratic fit illustrates scaling of dark current with device area.

Additionally, for the data presented in Figure 17, the scaling of dark current at low gains with device diameter exhibits quadratic behavior, as seen in Figure 18, indicating that surface leakage is minimal and dark current is likely to be dominated by bulk leakage from the superlattice absorption region.

Finally, the compatibility of this hole injection structure with our fabrication platform for planar geometry devices will allow us to efficiently translate this initial proof-of-concept success to the highly reliable and manufacturable device process flow in which we use planar dielectric passivation and dopant diffusion to form buried p-n junctions. We have already completed the epitaxial growth of the hole injection (InP multiplication region) structure with a thick (4 μm) undoped cap layer to accommodate our Zn diffusion process for creating p-n junctions. The fabrication of these planar geometry devices and the comparison of their performance characteristics (especially dark current) with the mesa geometry samples already characterized will be a near-term activity in the continuation of this program.

3.5 Temperature-dependent APD gain simulations

As mentioned briefly in Section 2 with reference to the electron injection APD results, the design of the APD charge distribution and the resulting internal electric field profile generally needs to be optimized for a specific range of operating temperatures. This arises because the impact ionization process is temperature-dependent and must be described by temperature-dependent ionization coefficients. Physically, the origin of this temperature dependence is related to the phonon scattering probability for carriers being accelerated in the multiplication region. At lower temperatures, the reduction in phonon scattering events allows carriers to be achieve sufficient kinetic energy for impact ionization at a lower internal electric field amplitudes. Therefore, for a given field, higher gains will be obtained at lower temperature. (This phenomenon also explains the decrease in breakdown voltage with lower temperatures.)

We have incorporated temperature-dependent impact ionization coefficients into the local field model mentioned in the previous section for our simulation of APDs with InP multiplication regions. The temperature dependence of InP material parameters has been sufficiently well-studied that we have been able to find reasonable agreement among different authors after surveying the technical literature. We are also in the process of trying to find comparable data for the temperature dependence of impact ionization coefficients in AlInAs so that we can carry out similar calculations for the electron injection structures and compare these with experimental data.

4. Modeling of GaInAs/GaAsSb Type-II Heterostructure using Model Solid Theory

Another enormous advantage of the GaInAs/GaAsSb Type-II SL structure is that the composition can be changed to allow tuning of the detector cutoff wavelength over the entire MWIR wavelength range from 2.5 to 5 μm. As part of our Phase I effort, we have modeled the $Ga_xIn_{1-x}As/GaAs_ySb_{1-y}$ heterostructure using the Model Solid Theory[4] to calculate the expected detection wavelength cutoff. The Model Solid Theory also allows for computation of the effects of epitaxial strain on the conduction and valence bands of the materials. Once that information is found for a particular (x,y) combination (dictating the precise stoichiometry of the $Ga_xIn_{1-x}As/GaAs_ySb_{1-y}$ superlattice, the band offsets and Type-II band gap energy can be determined. The appropriate equations for these quantities are:

$$\Delta E_C = E_c^{GaAsSb} - E_C^{GaInAs} \tag{1a}$$

$$\Delta E_V = E_V^{GAsSb} - E_V^{GaInAs} \tag{1b}$$

$$E_G^{type-II} = E_c^{GaInAs} - E_V^{GaAsSb} \tag{1c}$$

To test the applicability of this technique, the Type-II bandgap of $Ga_{0.47}In_{0.53}As/GaAs_{0.51}Sb_{0.49}$ was modeled. For room temperature parameter values, the calculated Type-II band gap was 492 meV (corresponding to a cutoff wavelength of 2.52 μm) using Eq. (1c) above. When quantization effects are considered, the detection wavelength from the modeling and experiment agree well (cf. experimental results in Figures 5 and 6). The model has been extended to include materials with epitaxial strain within 2% of an InP substrate. We expect to achieve very high quality material with the targeted low strains of no greater than 2% since, in earlier work, Profs. Holmes and Campbell at UT-Austin have shown shorter wavelength, high performance p-i-n and avalanche photodiodes on GaAs substrates using GaAsSb with more than 2% strain[6,7].

Table 1 shows the expected band gap energies for different combinations of strain in the GaInAs and GaAsSb layers. In this table, compressive strain is positive and tensile strain is negative. For the longest wavelengths, a combination of compressively strained GaAsSb and tensile strained GaInAs is required. Since the strain in the superlattice layers alternates, strain compensation can be used to allow for the growth of thick absorption regions to provide high quantum efficiencies and detectivities.

Table 1: Expected Room Temperature Type-II Band Gap Energy and Band Gap Wavelength for various compositions of GaInAs/GaAsSb heterostructures. Compressive strain is positive (+) and tensile strain is negative (-).

GaInAs/GaAsSb Compositions	GaInAs Strain	GaAsSb Strain	Type-II Band Gap Energy (meV)	Type-II Band Gap Wavelength (μm)
$Ga_{0.47}In_{0.53}As/GaAs_{0.51}Sb_{0.49}$	0%	0%	492	2.52
$Ga_{0.61}In_{0.39}As/GaAs_{0.38}Sb_{0.62}$	-1%	+1%	419	2.96
$Ga_{0.68}In_{0.32}As/GaAs_{0.31}Sb_{0.69}$	-1.5%	+1.5%	378	3.28
$Ga_{0.54}In_{0.46}As/GaAs_{0.31}Sb_{0.69}$	-0.5%	+1.5%	323	3.84
$Ga_{0.61}In_{0.39}As/GaAs_{0.24}Sb_{0.76}$	-1%	+2%	286	4.34
$Ga_{0.54}In_{0.46}As/GaAs_{0.24}Sb_{0.76}$	-0.5%	+2%	253	4.91

We have already shown that the preliminary calculations of the predicted detection cutoff wavelength of the $Ga_xIn_{1-x}As/GaAs_ySb_{1-y}$ heterostructure system using the Model Solid Theory agree well with the spectral response data obtained for the lattice-matched $Ga_{0.47}In_{0.53}As/GaAs_{0.51}Sb_{0.49}$ absorbers characterized in p-i-n structures. Table 1 shows how strain compensation can be used to allow for the growth of thick absorption regions to provide high quantum efficiencies and detectivities. For instance, the composition shown in row 2 of Table 1 is predicted to have a cutoff wavelength of 2.96 μm after introducing alternating strains of

+1% and −1%. By using GaInAs and GaAsSb layers of identical thickness, the strain is precisely compensated. Row 3 illustrates a composition for achieving a 3.28 μm cutoff through the use of compensated 1.5% strain.

In Row 5 of Table 1, we include a composition in which the tensile −1% strain in the GaInAs must be accompanied by compressive +2% strain in the GaAsSb. To achieve strain compensation in this case, the GaAsSb layers must be half the width of the GaInAs layers. This situation is fortuitous since a wider GaInAs layer will provide mini-band states for the electrons that are closer to the conduction band (as in the limit of a wide quantum well), while a narrower GaAsSb layer can be tolerated since the mini-band states for the relatively heavier holes will remain near the valence band. According to the model, the resulting structure will provide a cutoff wavelength beyond 4.3 μm.

There are numerous aspects of this modeling to be explored in greater detail since there are many physical properties of these SL structures to be optimized. Aside from the effective bandgap, which dictates the cutoff wavelength, the SL design will impact other critical parameters such as the material absorption coefficient (which depends on the degree of overlap between the electron and hole wavefunctions) and the carrier collection efficiency (which depends on the degree of overlap between quasi-localized carrier wavefunctions in neighboring wells). The absorption coefficient and carrier collection efficiency both directly impact the overall quantum efficiency of the resulting detector. Nevertheless, despite these opportunities for a more thorough understanding this SL system, the promise of designing MWIR APDs with it has already been demonstrated by the results of our Phase I effort.

5. Technological Feasibility for MWIR APDs based on InP Substrates

We believe there are several physical and technological factors inherent in the MWIR APD design pursued in this program that make this design extremely promising for high-performance MWIR detection at operating temperatures consistent with thermo-electric cooling. We have discussed the benefit of using a superlattice based on GaInAs and GaAsSb. The effective bandgap of the resulting superlattice can be tuned through the use of quantum confinement effects controlled by choice of layer thickness as well as through the introduction of compensated strain. Additionally, the relatively larger bandgaps of these two bulk materials (~0.75 eV at 300 K) should help to minimize leakage currents. For structures with a 2.5 μm SL cutoff, we have demonstrated low dark currents (10 − 100 nA) for both p-i-n and APD structures at temperatures accessible using thermoelectric coolers. These first iteration results suggest that further optimization will yield extremely high performance devices for ~2.5 μm devices, and we believe the prospects are good for achieving high performance devices well beyond 4 μm based on the results of our SL modelling.

Aside from the promise of high performance described in detail earlier in this report, it is of great significance that the superlattice structure studied is lattice-matched to InP substrates. This compatibility with an InP materials systems is extremely significant for the following reasons:

(i) Applicability of present InP lattice-matched multiplication regions. The ability to use InP substrates with MWIR absorbers will allow us to employ very well-understood multiplication region designs. The most widely deployed multiplication region used in III-V semiconductor APDs is binary InP itself. Although other materials have been studied in recent years to develop

lower noise, higher gain-bandwidth product multiplication regions, InP is still by far the most technologically mature material used for III-V APD multiplication regions. Scientists at PLI have nearly 10 years of experience designing and fabricating commercial APDs for telecommunications wavelengths based on InP multiplication regions, and we expect that the first commercially viable MWIR APD will be realized using a similar design approach. For further improvements in device performance, there is a clear path through the implementation of more favorable bulk materials, such as InAlAs lattice-matched to InP, or through the use of impact ionization engineered multiplication regions pioneered by the UT-Austin investigators on this program.

(ii) Leverage advances in InP-based epi-growth over the past decade. Tremendous improvements have been realized in recent years in the epi-growth quality of the InP-based materials systems. Commercial vendors routinely achieve sub-1% variations in epi-layer thickness across an entire 3-inch InP wafer and have shrunk their tolerances on all growth parameters considerably. Material quality has already improved substantially, as measured by the reduction in background doping densities of typical growth runs today by almost an order of magnitude relative to typical growth results from just five to ten years ago.

(iii) Mature wafer foundry capabilities for processing InP-based structures. In particular, the maturity of key processes for realizing high-quality planar passivated diffused p-n junction photodetectors gives devices manufactured on this platform low dark current, long-term performance stability, and high reliability. The re-use of other existing materials and processes, including high-quality dielectrics (e.g., SiN) and contact metallizations (e.g., TiPtAu p-contacts and AuGeNiAu n-contacts), also builds confidence in the viability of MWIR APDs based on these platform processes.

(iv) Availability of high-quality 4-inch InP substrates. The migration of a new MWIR detector technology to array formats will be greatly facilitated by the availability of high-quality large diameter substrates. The use of larger InP substrates provides an obvious economy of scale for large dimension detector arrays; but it also provides a less obvious, though very substantial, improvement in device yield and overall quality since more precise processes and tools (such as projection lithography and cassette-to-cassette robotic handling) are much more readily available for processing 4-inch wafers.

6. Researchers involved in Phase I program activities

At Princeton Lightwave:

>   Dr. Mark Itzler, Principal Investigator
>
>   Dr. Jeff Hsu, Principal Scientist
>
>   Krystyna Slomkowski, Senior Staff Engineer

At University of Texas at Austin

>   Prof. Archie Holmes
>
>   Prof. Joe Campbell
>
>   Rubin Sidhu, Research Associate
>
>   Ning Duan, Research Associate

References

[1] J.-X. Fu, S. R. Bank, M. A. Wistey, H. Yuen, and J. James S. Harris, "Solid-source molecular-beam epitaxy growth of GaInNAsSb/InGaAs single quantum well on InP with photoluminescence peak wavelength at 2.04 μm," *Journal of Vacuum Science & Technology B (Microelectronics Processing and Phenomena)*, vol. 22, pp. 1463-1467, 2004.

[2] M. R. Gokhale, J. Wei, H. Wang, and S. R. Forrest, "Growth and characterization of small band gap (~ 0.6 eV) InGaAsN layers on InP," *Applied Physics Letters*, vol. 74, pp. 1287-1289, 1999.

[3] J. C. Dries, M. R. Gokhale, and S. R. Forrest, "A 2.0 mm cutoff wavelength separate absorption, charge, and multiplication layer avalanche photodiode using strain-compenstated InGaAs quantum wells," *Applied Physics Letters*, vol. 74, pp. 2581-2583, 1999.

[4] C. G. V. d. Walle, "Band Lineups and Deformation Potentials in the Model-Solid Theory," *Physical Review B*, vol. 39, pp. 1871-1883, 1989.

[5] S. R. Forrest, R. F. Leheny, R. E. Nahory, and M. A. Pollack, "$In_{0.53}Ga_{0.47}as$ Photo-Diodes with Dark Current Limited by Generation-Recombination and Tunneling," *Applied Physics Letters*, vol. 37, pp. 322-325, 1980.

[6] X. Sun, J. Hsu, X. G. Zheng, J. C. Campbell, and J. A. L. Holmes, "GaAsSb Resonant-Cavity-Enhanced Photodetector Operating at 1.3 mm," *IEEE Photonics Technology Letters*, vol. 14, pp. 681, 2002.

[7] X. Sun, S. Wang, J. S. Hsu, R. Sidhu, X. G. Zheng, Xiaowei Li, J. C. Campbell, and J. Archie L. Holmes, "GaAsSb: A Novel Material for Near Infrared Photodetectors on GaAs Substrates," *IEEE Journal of Selected Topics in Quantum Electronics*, vol. 8, pp. 817, 2002.